SCIENCE CHINA Materials

ARTICLES

mater.scichina.com link.springer.com

Published online 9 May 2019 | https://doi.org/10.1007/s40843-019-9431-4
Sci China Mater 2019, 62(9): 1275–1284

Morphological and structural engineering in amorphous Cu_2MoS_4 nanocages for remarkable electrocatalytic hydrogen evolution

Jian Yu, Anran Li, Lidong Li, Xiaoxia Li, Xiaotian Wang and Lin Guo*

ABSTRACT Morphological and structural control of amorphous nanomaterials is challenging due to the long-range disordered atomic arrangements. Herein, we firstly propose a controllable self-hydrolyzing etching-precipitating (SHEP) method to fabricate the regular-shaped amorphous Cu_2MoS_4 nanocages (a-Cu_2MoS_4 NCs) with hollow porous structures under ambient conditions. Benefitting from the hollow porous structures and the amorphous characteristics with copious sulfur vacancies, the a-Cu_2MoS_4 NCs possess more enhanced activity toward hydrogen evolution reaction (HER) than their crystalline counterparts. The octahedral a-Cu_2MoS_4 NCs with a shell thickness of 20 nm, which balance the appropriate surface porosity and good structural stability, exhibit the best HER activity with a low overpotential of 96 mV at 10 mA cm^{-2} and a small tafel slope of 61 mV decade^{-1} in alkaline environment. Moreover, this method is very versatile and can be extended to synthesize other ternary nanocages. Our current work may shed light on the precise controllable synthesis of various ternary nanocages and open a new frontier for developing highly active amorphous catalysts.

Keywords: amorphous nanomaterials, nanocages, hollow structures, electrocatalysis, hydrogen evolution reaction

INTRODUCTION

Recently, amorphous nanomaterials have attracted more and more attention as a promising electrocatalyst for hydrogen evolution reaction (HER) [1–4]. Compared with their crystalline counterparts, amorphous nanomaterials feature distinctive long-range disordered but short-range ordered atomic arrangements, isotropic physical and chemical properties, while accommodating abundant intrinsic defects [5–8]. Simultaneously, the defect sites of nanomaterials play an important role in promoting the electrocatalytic reaction [9–11]. These characters endow amorphous nannomaterials with more flexible structure and higher active site density [12–15], resulting in higher electrocatalytic activity than their crystalline counterparts. A pioneering study by Hu and co-workers [16] revealed that amorphous MoS_x catalysts have superior HER activities compared with crystalline MoS_2. The high catalytic activity results from the inherent surface defect sites of amorphous MoS_x, i.e., coordinately and structurally unsaturated sulfur atoms [17], which were subsequently confirmed by *in situ* Raman spectroscopy and X-ray absorption spectroscopy (XAS) [18,19]. Besides, Kornienko *et al.* [13] demonstrated that amorphous CoS_x exposed a higher density of catalytic active sites leading to better HER performance than bulk CoS_2. Similar results were also obtained from amorphous tungsten phosphide and molybdenum phosphide nanoparticles [20,21], as well as other excellent catalysts with amorphous structures [22–24].

Moreover, the catalytic activity of amorphous nanomaterials could be further improved through the rational design of their structures. Unique hollow-structured nanomaterials have garnered tremendous research interests due to their structural advantages such as large specific surface area, low density, high pore volume, and reduced mass-/charge-transport lengths [25–27]. To date, numerous synthetic strategies for hollow-structured materials have been developed based on diverse methods such as Kirkendall effect [28,29], Ostwald ripening [30], ionic exchange [31,32], coordinating etching [33], galvanic replacement [34,35], and self-assembly [36]. Nevertheless, the regular-shaped ternary hollow nanomaterials with amorphous feature are rarely reported owing to the disordered atomic arrangement of their internal structures

School of Chemistry, Key Laboratory of Bio-Inspired Smart Interfacial Science and Technology, Ministry of Education, Beijing Advanced Innovation Center for Biomedical Engineering, Beihang University, Beijing 100191, China
* Corresponding author (email: guolin@buaa.edu.cn)

and poor mechanical stability. Furthermore, compared with binary hollow-structured materials (e.g., metal oxides or sulfides), the ternary hollow nanostructures may have more merits arising from the synergy effect by the introduction of extra atoms [37,38], leading to optimized electronic structure, better conductivity and enhanced HER performance [39], such as the reported $NiCo_2O_4$ [40], Co-Mn-O [41], $NiMo_3S_4$ [42], and $NiCo_2S_4$ [43].

Inspired by above the considerations, we herein develop a self-hydrolyzing etching-precipitating (SHEP) method to synthesize the regular-shaped ternary amorphous Cu_2MoS_4 nanocages (a-Cu_2MoS_4 NCs) with controllable shapes, sizes, and shell thicknesses for the first time (Scheme 1). The a-Cu_2MoS_4 NCs exhibit better HER performance than their crystalline counterparts, which can be ascribed to two main advantages: 1) amorphous features with disordered atomic arrangements and inherent abundant defects endow the a-Cu_2MoS_4 NCs with a large number of sulfur vacancies, which is conducive to the fluent diffusion of protons; 2) unique hollow porous structure gives the a-Cu_2MoS_4 NC a larger specific surface area, more accessible active sites, and favorable electrons/ions transport in the electrolyte. Interestingly, the electrocatalytic performance of the a-Cu_2MoS_4 NCs is closely related to their shell thickness—the octahedral a-Cu_2MoS_4 NCs with a shell thickness of 20 nm exhibit the best HER activity with the overpotential as low as 96 mV at 10 mA cm^{-2} and the Tafel slope of 61 mV decade^{-1}. In addition, compared with the traditional method for synthesizing hollow nanomaterials, our method simplifies the experimental procedure and is self-sufficient, without additional coordinating agent or etching agent, and can be performed at room temperature. Importantly, our method can be extended to the synthesis of other ternary NCs, which are expected to be applied in other fields.

EXPERIMENTAL SECTION

Synthesis of solid Cu_2O templates

The spherical Cu_2O, cubic Cu_2O and octahedral Cu_2O with different sizes were prepared according to our previous work [44,45]. And the morphologies of Cu_2O samples are shown in Figs S1–S5.

Synthesis of a-Cu_2MoS_4 NCs

In a typical synthesis, 5.0 mg Cu_2O octahedrons (600 nm) were first dispersed in 5 mL ethanol and sonicated for

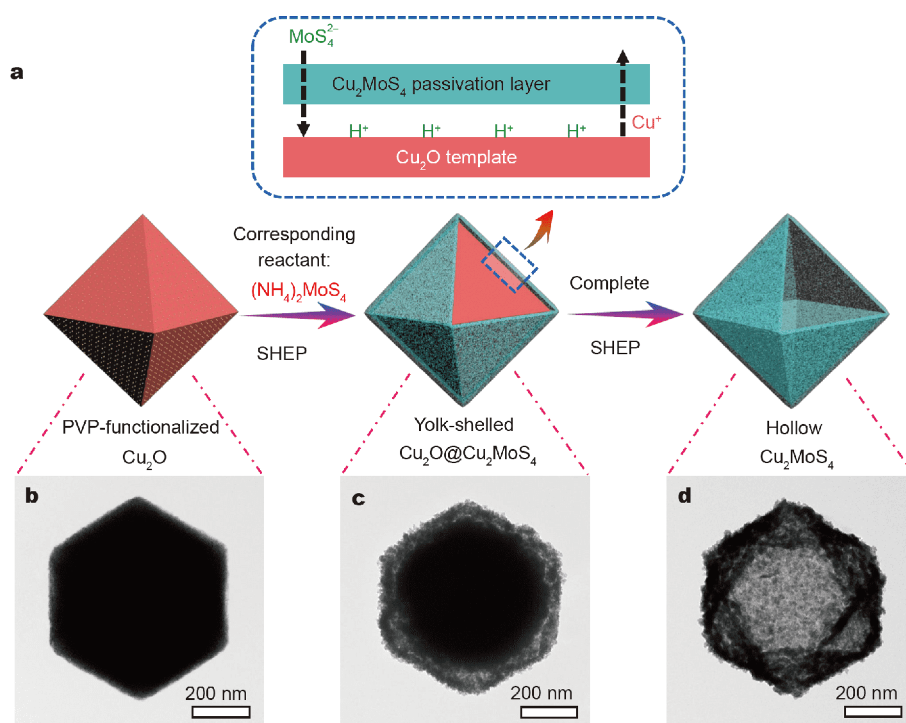

Scheme 1 The formation process of ternary amorphous NCs by SHEP method: (a) schematic illustration of the synthesis procedure for a representative octahedral a-Cu_2MoS_4 NCs. The representative TEM images of the Cu_2O solid octahedron (b), $Cu_2O@Cu_2MoS_4$ yolk-shelled structure (c) and hollow Cu_2MoS_4 NC (d).

2 min. Then, 20 mL H_2O, 20 mL ethanol and 0.05 mmol polyvinyl pyrrolidone (PVP) were added and kept magnetic stirring. Finally, 2.8 mL $(NH_4)_2MoS_4$ (7.68 mmol L^{-1}) aqueous solution (the solution was freshly prepared just before use) was added dropwise into the above solution. The reaction was carried out for 1.5 h at room temperature. The octahedral a-Cu_2MoS_4 NCs were collected by centrifugation at 8,000 rpm and decanted, washed with distilled water and ethanol several times, and subsequently dried in a vacuum oven at 50°C for 12 h. The as-prepared a-Cu_2MoS_4 NCs have a size of 600 nm and a thickness of 20 nm (labeled as a-Cu_2MoS_4 NCs-20). Cu_2MoS_4 NCs with other morphologies, such as spheres, cubes, or octahedrons with different thicknesses were obtained with the same method with different Cu_2O templates/amounts of reactants/reaction times (see Table S1). The reactions are described by the following Equations (1–4):

$$(NH_4)_2MoS_4 \rightarrow 2\ NH_4^+ + MoS_4^{2-}, \quad (1)$$

$$NH_4^+ + H_2O \rightleftharpoons H^+ + NH_3{\cdot}H_2O, \quad (2)$$

$$Cu_2O + 2H^+ \rightarrow 2Cu^+ + H_2O, \quad (3)$$

$$2Cu^+ + MoS_4^{2-} \rightarrow Cu_2MoS_4 \downarrow. \quad (4)$$

Electrochemical measurements

Electrochemical measurements were performed on a CHI 660E electrochemical workstation (Shanghai Chenhua, China) using a standard three-electrode cell with a working electrode, a graphite rod as counter electrode, and a saturated Ag/AgCl electrode as reference electrode. All the potentials reported in this study are referenced to the reversible hydrogen electrode (RHE) by adding a value of (0.197+0.0591pH) V. KOH (0.1 mol L^{-1}) solution (pH 13) was selected as the electrolyte solution during the whole process. The working electrode was prepared by a similar method reported in the literature [46]: 5 mg catalyst sample was dispersed in a mixed solution containing 700 μL of deionized water, 270 μL of ethanol and 40 μL of 5 wt% Nafion solution. And the mixture was ultrasonicated for 20 min to generate a homogeneous ink. Then 300 μL of the as-prepared ink was dropped onto Ni foam (1 cm×1 cm) and left to air dry. The mass loadings of the catalysts were 1.48 mg cm^{-2}. Linear sweep voltammetry (LSV) was recorded with a scan rate of 10 mV s^{-1} in 0.1 mol L^{-1} KOH solution (purged with pure N_2 for 30 min). The electrochemical active surface areas (ECSA) were determined by cyclic voltammetry measurements at various scan rates ranging from 40 to 120 mV s^{-1} in the potential window of 0.12–0.32 V *versus* RHE. The electrochemical impedance spectra (EIS) were obtained by alternate current (AC) impedance spectroscopy in 0.1 mol L^{-1} KOH solution with 5 mV amplitude, and frequency range from 1 Hz to 100 kHz at an overpotential of 200 mV (*vs.* RHE). All the above measurements were performed at room temperature, and without ohmic-drop correction.

Density functional theory (DFT) calculations

The DFT computations were performed using the Vienna *ab initio* simulation package (VASP v.5.4.1) [47,48]. During all calculations, the generalized gradient approximation and the projector augments wave pseudopotentials with the exchange and correlation in the Perdew-Burke-Ernzerhof were employed [49,50]. The plane-wave cutoff energy is set at 400 eV. The convergence threshold was set as 10^{-5} eV in energy and 0.02 eV $Å^{-1}$ in force, respecively. The Monkhorst-Pack Gamma-centered *k*-points mesh is adopted for all calculations, where the spacing of uniformly sampled *k* points for each simulation was set to be no larger than $2\pi\times0.03$ $Å^{-1}$. The crystalline (c-MoS_2) and the crystalline Cu_2MoS_4 (c-Cu_2MoS_4) models were built based on the lattice parameters of 2H MoS_2 with the hexagonal crystal system and I-Cu_2MoS_4 with a tetragonal ($I\bar{4}2m$) symmetry [51], respectively (Figs S20–S21). The a-Cu_2MoS_4 NCs-20 is different from c-Cu_2MoS_4 due to long-range atomic disorder and sulfur vacancies (Fig. S22). Therefore, it was built by randomly deleting one sulfur atom per unit cell of c-Cu_2MoS_4. For computing the hydrogen adsorption energy, layer slab models of (3 x 3) c-MoS_2 (001), (2 x 2) c-Cu_2MoS_4 (001), and (2 x 2) a-Cu_2MoS_4 (001) were constructed respectively with a vacuum layer of 15 Å. For geometry optimizations of all slab models, the top two layers were allowed to relax. The free energy of the adsorbed state is calculated as:

$$\Delta G(H^*) = \Delta E(H^*) + \Delta EZPE - T{\cdot}\Delta S, \quad (5)$$

where $\Delta E(H^*)$ is the hydrogen binding energy, and ΔEZPE is the difference corresponding to the zero point energy between the adsorbed state and the gas phase. As the vibrational entropy of H* in the adsorbed state is small, the entropy of adsorption of 1/2 H_2 is $\Delta S(H) \approx -0.5\, S(OH_2)$, where $S(OH_2)$ is the entropy of H_2 in the gas phase at the standard conditions. Therefore the overall corrections are taken as

$$\Delta G(H^*) \approx \Delta E(H^*) + 0.24\ eV. \quad (6)$$

RESULTS AND DISCUSSION

Characterization and formation process of the a-Cu_2MoS_4 NCs

Scheme 1a illustrates the structural formation processes of ternary amorphous NCs by SHEP method, and the synthetic details are given in the EXPERIMENTAL SECTION. For the convenience of presentation, we take the octahedral a-Cu_2MoS_4 NCs sample as an example. Firstly, the uniform Cu_2O solid octahedrons with the edge length of 600 nm (Fig. S1, Scheme 1b) were prepared and redispersed in a solution of PVP as the templates. Then $(NH_4)_2MoS_4$ was as a reactant, which can be used as both an etchant and a precipitant. At the initial stage of the SHEP process, $(NH_4)_2MoS_4$ can be dissolved in water to release NH_4^+ and MoS_4^{2-} (Equation 1). The NH_4^+ ion is a conjugate acid of ammonia, which can be hydrolyzed to produce H^+ and $NH_3{\cdot}H_2O$ (Equation 2). These hydrolyzed H^+ ions trigger the etching of Cu_2O hard templates to release Cu^+ ions (Equation 3). At the same time, an insoluble passivation layer of Cu_2MoS_4 species easily forms *in-situ* on the surface of Cu_2O templates due to thermodynamically favorable precipitation reaction between MoS_4^{2-} and Cu^+ (Equation 4). The continuous consumption of Cu_2O core results in a small gap between the newly formed Cu_2MoS_4 shell and the remaining Cu_2O core, and the obtained $Cu_2O@Cu_2MoS_4$ yolk-shelled structures are confirmed by the scanning electron microscopy (SEM) image (Fig. S2) and transmission electron microscopy (TEM) image (Scheme 1c). Eventually, as the SHEP reaction prolongs, the complete depletion of interior core results in the formation of the robust octahedral a-Cu_2MoS_4 NCs (Scheme 1d). Compared with the conventional templating method that requires an extra coordination agent or an etching agent to remove the template [26], SHEP does not need the additional coordination agent or etching agent due to the dual functionality of the reactant $(NH_4)_2MoS_4$ during the overall process. Besides, SHEP also distinguishes itself from the reported self-templating strategies based on different principles such as the Kirkendall effect, Ostwald ripening, galvanic replacement, and so on [29,30,35]. These strategies usually require heating aids or solvothermal processes, even not suitable for insoluble inert templates because they cannot provide free ions in solution [52]. Instead, our method simplifies the experimental procedures and provides a milder reaction condition that can be performed at room temperature.

As shown in Fig. 1a, the Cu_2MoS_4 nanoarchitectures well maintain the octahedral morphology of the original template of Cu_2O and are very uniform with an average edge length of 600 nm. However, their surfaces are changed from a smooth surface of Cu_2O templates (Fig. S1a) to a rough porous surface (Fig. S3a, b) due to the outward flow of internal ions. The corresponding

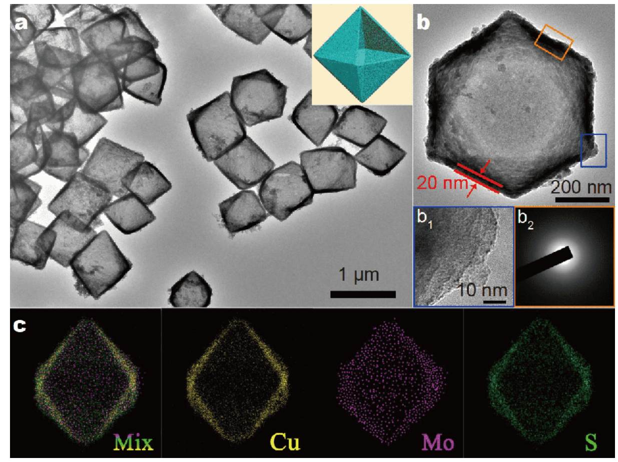

Figure 1 (a) Overview TEM, (b) magnified TEM, (b_1) HRTEM images, and (b_2) SAED pattern of the octahedral a-Cu_2MoS_4 NCs, inset in (a) shows the 3D modeling structure. (c) EDS elemental mapping images for Cu, Mo, and S elements of the octahedral a-Cu_2MoS_4 NC.

TEM characterization demonstrates the large internal cavity with a uniform shell thickness of 20 nm (Fig. 1b) in each Cu_2MoS_4 NC by a clear contrast between the hollow interior and the external solid shell. Besides, relevant high-resolution TEM (HRTEM) image (Fig. 1b_1) with no lattice fringes and selected area electron diffraction (SAED) pattern (Fig. 1b_2) with a scattered and hazy halo indicate the amorphous nature of the octahedral Cu_2MoS_4 NCs. The amorphous structure is also evidenced by the X-ray power diffraction (XRD) pattern with no distinct diffraction peaks (Fig. S4a). The energy-dispersive X-ray spectroscopy (EDS) result indicates Cu, Mo, and S in the octahedral a-Cu_2MoS_4 NCs with Cu/Mo/S atomic ratio of about 2:1:4 (Fig. S3c), and the EDS elemental mapping of a single octahedral a-Cu_2MoS_4 NC reveals the presence and uniform distribution of Cu, Mo, and S (Fig. 1c). The chemical compositions and states of the as-prepared octahedral a-Cu_2MoS_4 NCs are further confirmed by the X-ray photoelectron spectroscopy (XPS). The Cu $2p_{3/2}$ and Cu $2p_{1/2}$ binding energies of a-Cu_2MoS_4 NCs locate at 933.0 and 953.0 eV, respectively (Fig. S4b), which indicate that the Cu species in a-Cu_2MoS_4 NCs are monovalent [53,54]. The peaks at 229.9 and 233.0 eV correspond to Mo $3d_{5/2}$ and Mo $3d_{3/2}$ (Fig. S4c) respectively, indicating molybdenum as the Mo(VI) oxidation state [53,54]. The peaks of S $2p_{3/2}$ and S $2p_{1/2}$ at 161.5 and 162.6 eV, respectively (Fig. S4d), can be assigned to S(II) species [51]. All of the above results indicate the successful synthesis of the octahedral a-Cu_2MoS_4 NCs.

Controllability and universality of SHEP method

In order to demonstrate the precise controllability of our synthetic strategy (Fig. 2), the a-Cu_2MoS_4 NCs with different thicknesses, sizes and morphologies were synthesized by SHEP method. It is well known that the amount of reactants is an important factor in chemical synthesis. We found that the thickness of NCs can be easily and accurately controlled by the amount of reactants. For example, the octahedral a-Cu_2MoS_4 NCs with a thickness of 20 nm can be synthesized (Fig. 1) by using 2.8 mL $(NH_4)_2MoS_4$ (7.68 mmol L^{-1}). While, increasing $(NH_4)_2MoS_4$ volume to 3.2 mL, the octahedral a-Cu_2MoS_4 NCs with a thickness of 30 nm can be obtained (Fig. 2b_1, b_2). However, the octahedral hollow structures will not be maintained if the volume of reactants continues to increase (>3.2 mL) (Fig. S6b). It might be explained by that a thick outer shell formed by excessive precipitates leads to the filling of the inner cavity. In contrast, the thinner octahedral a-Cu_2MoS_4 NCs with a thickness of 10 nm can also be prepared (Fig. 2a_1, a_2) by reducing the volume of $(NH_4)_2MoS_4$ to 2.4 mL. Compared with the octahedral a-Cu_2MoS_4 NCs with 20 and 30 nm thicknesses, the a-Cu_2MoS_4 NCs with 10 nm thickness are more likely to crack, and the extent of rupture is greater (Fig. 2a_1). We can hardly obtain the whole octahedral a-Cu_2MoS_4 NC if we continue to reduce the volume of $(NH_4)_2MoS_4$ (<2.4 mL) (Fig. S6a). Because the surface support force of the shell is not big enough due to the small shell thickness, resulting in the octahedral hollow frames invaginated or even completely collapsed. The porous structures of a-Cu_2MoS_4 NCs surface become less obvious with the increase of thickness (Figs S7a, S3b, S7b), and when the thickness of the shell becomes too thick, no porous structure can be observed on the surface (Fig. S6b). Therefore, the NCs with a suitable shell thickness not only maintain the structural robustness but also the porosity of their surface, which may help to enhance their catalytic properties and is in favor of the practical application of hollow structural materials [55]. For example, the hollow nanomaterials with porous shells can be used both as nanoreactors for catalytic reaction and nanocontainers for the drug storage and release [56–58]. In addition, the size of NCs can also be effectively controlled by using templates with different sizes. Using Cu_2O octahedrons with the edge lengths of 400 and 800 nm, (Fig. S5a, b), the octahedral a-Cu_2MoS_4 NCs with dimensions of about 400 and 800 nm can be successfully prepared, respectively (Figs 2c_1, c_2 and 2d_1, d_2). Moreover, the morphologies of NCs are not limited to octahedron, the spherical and cubic Cu_2MoS_4 NCs can also be easily fabricated based on the SHEP method by using Cu_2O templates with corresponding morphologies. As shown in Figs 2e_1, e_2 and 2f_1, f_2, the resulting spherical Cu_2MoS_4 NCs have a diameter of about 600 nm and the cubic Cu_2MoS_4 NCs have a side length of about 600 nm, all of which are very uniform with hollow structures.

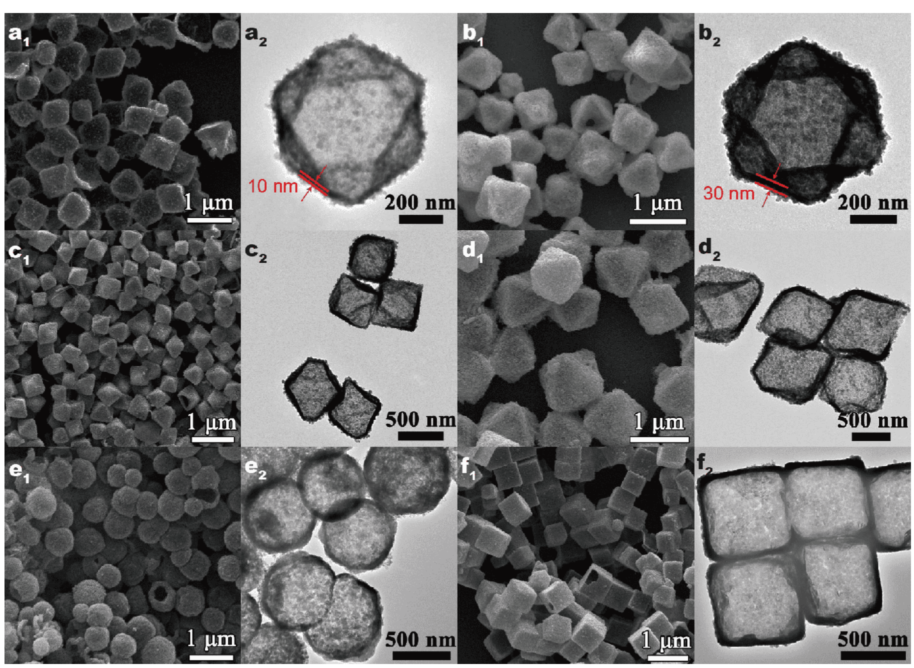

Figure 2 SEM ((a–f)$_1$) and TEM ((a–f)$_2$) images of a-Cu_2MoS_4 NCs with different shell thicknesses, different sizes, and different morphologies. The shell thicknesses are 10 (a_1, a_2) and 30 nm (b_1, b_2), respectively. The sizes are 400 (c_1, c_2) and 800 nm (d_1, d_2), respectively. The NCs are spherical (e_1, e_2) and cubic (f_1, f_2) in shape.

Furthermore, the role of surfactant PVP during the synthesis was also investigated by a control experiment. In the absence of PVP, the a-Cu_2MoS_4 NCs with octahedral morphology can still be obtained except the formation of a few irregular particles (Fig. S8), indicating PVP has no effect on the formation mechanism of NCs, but it is helpful to the uniformity of hollow structure. As previously reported [33], PVP can reduce the mobility of ions in solution, making the precipitate more prone to slow heterogeneous growth on the surface of the template rather than self-nucleation to grow into separate nanoparticles.

The SHEP method can be extended to synthesize many other ternary hollow nanostructures such as Cu_2MoO_4, Cu_2WS_4, and Cu_2WO_4 NCs (see Supplementary information S1.2 and Figs S9, S10) using their corresponding reactants such as $MoCl_5$, $(NH_4)_2WS_4$, and WCl_6. These corresponding reactants play two roles in the formation process of NCs: both as etchants and precipitants. These reactants all can undergo self-hydrolysis to produce acids. Then Cu_2O hard templates can be first etched by these H^+ ions to release Cu^+ ions. On the other hand, another part of the ions originating from the reactants acts as precipitants to form the passivation layers on the Cu_2O surface and maintains the regular morphology of the templates. Self-hydrolyzing etching and precipitating reactions could occur almost simultaneously. If the reaction time is short, the yolk-shell structures will form. If the reaction time is long enough to complete the SHEP reaction, the hollow structures can be obtained. The successful synthesis of various ternary NCs demonstrates the universality of our synthetic strategy.

HER performance and enhanced HER mechanism of a-Cu_2MoS_4 NCs

To demonstrate the advantages of the as-prepared amorphous and hollow structural NCs, the electrocatalytic performance for HER of the octahedral a-Cu_2MoS_4 NCs with different thicknesses were evaluated in 0.1 mol L^{-1} KOH solution with the same mass loading of 1.48 mg cm^{-2} on a Ni foam (1 cm×1 cm) electrode [46]. In Fig. 3a, the typical LSV curves for octahedral a-Cu_2MoS_4 NCs with different thicknesses of 10, 20, 30 nm (abbreviated as a-Cu_2MoS_4 NCs-10, a-Cu_2MoS_4 NCs-20 and a-Cu_2MoS_4 NCs-30, respectively) along with c-Cu_2MoS_4 NCs (see Fig. S11 for details), c-MoS_2, com-

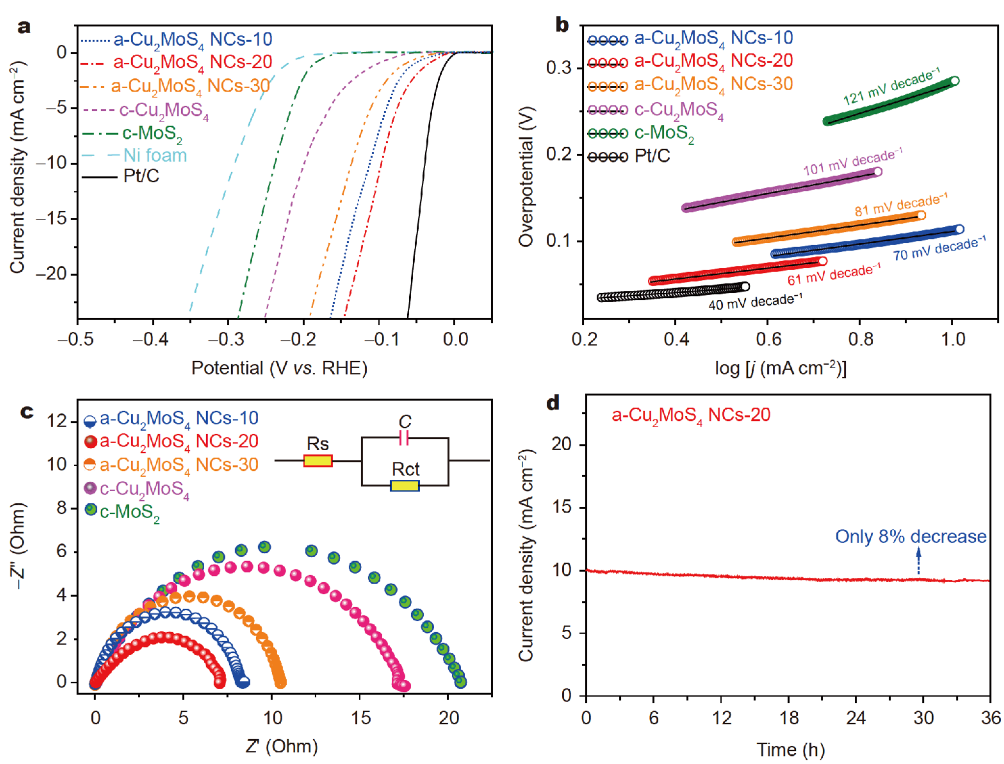

Figure 3 HER performance of the octahedral a-Cu_2MoS_4 NCs. (a) Polarization curves and (b) Tafel plots of a-Cu_2MoS_4 NCs-10, a-Cu_2MoS_4 NCs-20, a-Cu_2MoS_4 NCs-30, c-Cu_2MoS_4 NCs, c-MoS_2, Pt/C, and the bare Ni foam in 0.1 mol L^{-1} KOH. (c) Nyquist plots of a-Cu_2MoS_4 NCs-10, a-Cu_2MoS_4 NCs-20, a-Cu_2MoS_4 NCs-30, c-Cu_2MoS_4 NCs, c-MoS_2 at an overpotential of 200 mV; the inset shows the fitted equivalent circuit. (d) Chronoamperometry curve of a-Cu_2MoS_4 NCs-20 at a constant overpotential of 96 mV.

mercial 20% Pt/C and bare Ni foam are compared. As known, the overpotential at a current density of 10 mA cm^{-2} (defined as η_{10}) is a common criterion for HER performance (a metric associated with solar fuel synthesis) [59]. The a-Cu_2MoS_4 NCs-20 show the lowest overpotential of η_{10}=96 mV, which is even lower than that of many previously reported electrocatalysts based on metal sulfides and molybdenum-based catalysts (Table S3). Besides, the a-Cu_2MoS_4 NCs-10 and a-Cu_2MoS_4 NCs-30 require relatively higher overpotential: 112 and 136 mV, respectively, which are still lower than those of c-Cu_2MoS_4 NCs (η_{10}=198 mV), c-MoS_2 (η_{10}=237 mV) (detailed data in Table S2), crystalline CuS and Cu_2S (Fig. S12). It is suggested that the a-Cu_2MoS_4 NCs-20 have an overwhelming advantage in HER, which can be attributed to the hollow porous structures with the largest specific surface area (Fig. S13) and the amorphous characteristics with copious sulfur vacancies [60]. A sharp signal in electron paramagnetic resonance (EPR) spectra at g=2.027 provides a fingerprint evidence for the sulfur vacancies [61], and no obvious signal is detected for c-Cu_2MoS_4 NCs (Fig. S14). The a-Cu_2MoS_4 NCs-20 with a large amount of sulfur vacancies are favorable for fluent proton diffusion [60,62], leading to a better HER performance than c-Cu_2MoS_4 NCs. Moreover, NCs with a suitable thickness may have more prominent HER performance, because if the shell thickness is too thick, its surface will have less porous structure (Fig. S7b), which reduces the contact area between the electrodes and is not conducive to the transmission of electrons/ions in the electrolyte, resulting in poorer HER activity. In contrast, the NCs with smaller thickness, have a larger porous surface but their octahedral hollow structures are not robust enough, with more collapsing and incomplete structures (Fig. S6a), also resulting in a weaker HER activity. Therefore, the NCs with a suitable thickness balance the surface porosity and the structural stability, leading to outstanding HER activity. Besides, the a-Cu_2MoS_4 NCs-20 has the largest Brunauer-Emmett-Teller (BET) surface area of 67.4 m^2 g^{-1}, compared with all the other similar samples, such as a-Cu_2MoS_4 NCs-10, a-Cu_2MoS_4 NCs-30, c-Cu_2MoS_4 NCs, and c-MoS_2 (Fig. S13), also demonstrating that the amorphous NCs with a suitable thickness are significant to enhance HER performance.

To give insight into the origin of the improved activity, the ECSA of as-prepared samples were obtained by measuring the double-layer capacitance (C_{dl}), which was linearly proportional to ECSA (Figs S15–S19). The a-Cu_2MoS_4 NCs-20 sample has the highest C_{dl}, compared with a-Cu_2MoS_4 NCs-10, a-Cu_2MoS_4 NCs-30, c-Cu_2MoS_4 NCs, and c-MoS_2, suggesting that a-Cu_2MoS_4 NCs-20 has the most accessible active sites, which indicates the superior HER performance [52], and is in accordance with the above-mentioned results.

Furthermore, in order to evaluate the reaction kinetics of the catalysts, the HER Tafel plots were investigated (Fig. 3b). The linear regions of Tafel curves are plotted using the Tafel equation: $\eta=a + b\log(j)$, where a, b, and j are intercept, Tafel slope, and current density, respectively. As expected, the a-Cu_2MoS_4 NCs-20 exhibit the smallest Tafel slope of 61 mV $decade^{-1}$ compared with those of a-Cu_2MoS_4 NCs-10 (70 mV $decade^{-1}$), a-Cu_2MoS_4 NCs-30 (81 mV $decade^{-1}$), c-Cu_2MoS_4 NCs (101 mV $decade^{-1}$), and c-MoS_2 (121 mV $decade^{-1}$), revealing the excellent HER kinetics for a-Cu_2MoS_4 NCs-20, which is quite comparable with other reported electrocatalysts (Table S3). Moreover, the b of 61 mV $decade^{-1}$ implies that electrochemical desorption is the rate-determining step, following the Volmer-Heyrovsky mechanism (Fig. 4a) [63]. In addition, the EIS was also performed to further investigate the electrode reaction kinetics at an overpotential of η=200 mV. As shown in the Nyquist plots (Fig. 3c), the a-Cu_2MoS_4 NCs-20 exhibits the smallest charge transfer resistance (R_{ct}) of 7.1 Ω compared with those of a-Cu_2MoS_4 NCs-10 (8.3 Ω), a-Cu_2MoS_4 NCs-30 (10.5 Ω), c-Cu_2MoS_4 NCs (17.2 Ω), and c-MoS_2 (20.7 Ω), indicating a markedly fast Faradaic process and favorable HER kinetics [46]. It is mainly due to the fact that a-Cu_2MoS_4 NCs-20 has a suitable thickness shell that maintains both structural stability and rich surface porosity. As a result, the electrolyte can quickly penetrate into the hollow structure of NCs, and a larger electrochemical reaction surface area can be obtained, resulting in a small R_{ct}. In contrast, a thicker shell reduces the surface porosity, making it difficult for the electrolyte to penetrate into the interior of the NC, while a thinner shell is more likely to break, resulting in easier stacking. Both of them will lead to a relatively small electrochemical reaction surface area, resulting in a larger R_{ct}. This result again confirms that amorphous NCs with a suitable thickness not only provides more reactive sites but also improves the charge and mass transfer efficiency, which is in good agreement with the results of LSV curves and Tafel plots. In addition to the catalytic activity, long-term stability is another crucial criterion for the practical applicability of catalysts. Fig. 3d shows that a-Cu_2MoS_4 NCs-20 can maintain j=10 mA cm^{-2} for 36 h with only 8% reduction, corroborating the excellent durability of as-prepared catalyst.

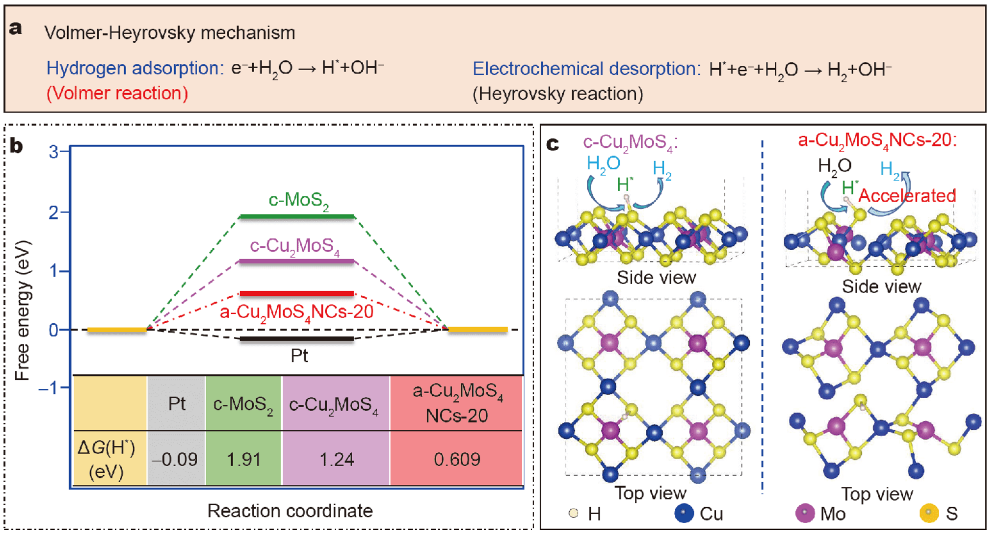

Figure 4 Gibbs free energy (ΔG) of H* adsorption and the corresponding mechanisms of the electrocatalytic HER. (a) A representative HER pathway by the Volmer-Heyrovsky mechanism. (b) Calculated free-energy diagram of catalyst samples. (c) Elucidation of the enhanced HER mechanism by the c-Cu_2MoS_4 and a-Cu_2MoS_4 NCs-20 models.

The DFT calculations have been performed to elucidate the mechanism of high electrocatalytic activity. The detailed parameters of models for the calculations are shown in the EXPERIMENTAL SECTION and Figs S20–S22. According to the Sabatier principle [64], a good catalyst should have a moderate free energy (ΔG) for H adsorption (H*), namely, ΔG(H*) close to zero, which is beneficial to both the adsorption process and the desorption process of hydrogen. As shown in Fig. 4b, the ΔG(H*) of c-MoS_2 is 1.91 eV, suggesting that the electrocatalytic HER process is not easy to be realized on the surfaces of c-MoS_2 due to the unfavourable interaction with H. The c-Cu_2MoS_4 NCs gives a ΔG(H*) of 1.24 eV, which is smaller than that of c-MoS_2, indicating that the introduction of Cu atoms might modulate the electronic potential distribution and electron density, enhancing the electrocatalytic activity for ternary catalysts [65]. The a-Cu_2MoS_4 NCs-20 lack long-range atomic order and possess the abundance of sulfur vacancies, resulting in a lower ΔG(H*) value (0.609 eV) than other systems, further accelerating HER performance (Fig. 4c), which is in good agreement with the experimental results discussed above.

CONCLUSIONS

In summary, a new and effective strategy is developed to fabricate the regular-shaped amorphous Cu_2MoS_4 NCs. The key feature of this strategy is that it involves a SHEP process, which simplifies the experimental procedures, provides mild reaction conditions, and avoids the usage of coordinating agents or etching agents. The controllability and versatility of this strategy enable the synthesis of various ternary NCs with tunable compositions, thicknesses, sizes, and morphologies. Benefiting from the amorphous characteristics with rich sulfur vacancies and hollow structures, the a-Cu_2MoS_4 NCs with an appropriate thickness exhibit greatly enhanced HER activity. We believe that our current work will offer an insight into the precise controllable synthesis of various ternary nanocages and is expected to be applied in different areas ranging from energy storage and conversion, catalysis, gas sensor, to drug delivery.

Received 5 March 2019; accepted 17 April 2019; published online 9 May 2019

1 Tran PD, Tran TV, Orio M, *et al.* Coordination polymer structure and revisited hydrogen evolution catalytic mechanism for amorphous molybdenum sulfide. Nat Mater, 2016, 15: 640–646
2 Masa J, Weide P, Peeters D, *et al.* Amorphous cobalt boride (Co_2B) as a highly efficient nonprecious catalyst for electrochemical water splitting: Oxygen and hydrogen evolution. Adv Energy Mater, 2016, 6: 1502313
3 Lee SC, Benck JD, Tsai C, *et al.* Chemical and phase evolution of amorphous molybdenum sulfide catalysts for electrochemical hydrogen production. ACS Nano, 2016, 10: 624–632
4 He W, Ifraemov R, Raslin A, *et al.* Room-temperature electrochemical conversion of metal-organic frameworks into porous amorphous metal sulfides with tailored composition and hydrogen evolution activity. Adv Funct Mater, 2018, 28: 1707244
5 Kang Y, Yang Y, Yin LC, *et al.* An amorphous carbon nitride photocatalyst with greatly extended visible-light-responsive range for photocatalytic hydrogen generation. Adv Mater, 2015, 27: 4572–4577

6 Liu J, Nai J, You T, *et al.* The flexibility of an amorphous cobalt hydroxide nanomaterial promotes the electrocatalysis of oxygen evolution reaction. Small, 2018, 14: 1703514
7 Zhang S, Dong D, Wang Z, *et al.* Spherical periodicity as structural homology of crystalline and amorphous states. Sci China Mater, 2018, 61: 409–416
8 Tang Y, Zhou P, Chao Y, *et al.* Face-to-face engineering of ultrathin Pd nanosheets on amorphous carbon nitride for efficient photocatalytic hydrogen production. Sci China Mater, 2019, 62: 351–358
9 Jia Y, Jiang K, Wang H, *et al.* The role of defect sites in nanomaterials for electrocatalytic energy conversion. Chem, 2019, doi: 10.1016/j.chempr.2019.02.008
10 Wang X, Zhuang L, Jia Y, *et al.* Plasma-triggered synergy of exfoliation, phase transformation, and surface engineering in cobalt diselenide for enhanced water oxidation. Angew Chem, 2018, 130: 16659–16663
11 Jia Y, Chen J, Yao X. Defect electrocatalytic mechanism: concept, topological structure and perspective. Mater Chem Front, 2018, 2: 1250–1268
12 Bennett TD, Cheetham AK, Fuchs AH, *et al.* Interplay between defects, disorder and flexibility in metal-organic frameworks. Nat Chem, 2016, 9: 11–16
13 Kornienko N, Resasco J, Becknell N, *et al. Operando* spectroscopic analysis of an amorphous cobalt sulfide hydrogen evolution electrocatalyst. J Am Chem Soc, 2015, 137: 7448–7455
14 Liu J, Ji Y, Nai J, *et al.* Ultrathin amorphous cobalt–vanadium hydr (oxy)oxide catalysts for the oxygen evolution reaction. Energy Environ Sci, 2018, 11: 1736–1741
15 Nai J, Kang J, Guo L. Tailoring the shape of amorphous nanomaterials: recent developments and applications. Sci China Mater, 2015, 58: 44–59
16 Merki D, Fierro S, Vrubel H, *et al.* Amorphous molybdenum sulfide films as catalysts for electrochemical hydrogen production in water. Chem Sci, 2011, 2: 1262–1267
17 Ge X, Chen L, Zhang L, *et al.* Nanoporous metal enhanced catalytic activities of amorphous molybdenum sulfide for high-efficiency hydrogen production. Adv Mater, 2014, 26: 3100–3104
18 Deng Y, Ting LRL, Neo PHL, *et al. Operando* Raman spectroscopy of amorphous molybdenum sulfide (MoS_x) during the electrochemical hydrogen evolution reaction: Identification of sulfur atoms as catalytically active sites for H^+ reduction. ACS Catal, 2016, 6: 7790–7798
19 Lassalle-Kaiser B, Merki D, Vrubel H, *et al.* Evidence from *in situ* X-ray absorption spectroscopy for the involvement of terminal disulfide in the reduction of protons by an amorphous molybdenum sulfide electrocatalyst. J Am Chem Soc, 2015, 137: 314–321
20 McEnaney JM, Chance Crompton J, Callejas JF, *et al.* Electrocatalytic hydrogen evolution using amorphous tungsten phosphide nanoparticles. Chem Commun, 2014, 50: 11026–11028
21 McEnaney JM, Crompton JC, Callejas JF, *et al.* Amorphous molybdenum phosphide nanoparticles for electrocatalytic hydrogen evolution. Chem Mater, 2014, 26: 4826–4831
22 Ren X, Wang W, Ge R, *et al.* An amorphous $FeMoS_4$ nanorod array toward efficient hydrogen evolution electrocatalysis under neutral conditions. Chem Commun, 2017, 53: 9000–9003
23 Li Y, Zhang H, Jiang M, *et al.* Amorphous Co–Mo–S ultrathin films with low-temperature sulfurization as high-performance electrocatalysts for the hydrogen evolution reaction. J Mater Chem A, 2016, 4: 13731–13735
24 Jin Z, Li P, Huang X, *et al.* Three-dimensional amorphous tungsten-doped nickel phosphide microsphere as an efficient electrocatalyst for hydrogen evolution. J Mater Chem A, 2014, 2: 18593–18599
25 Zhou L, Zhuang Z, Zhao H, *et al.* Intricate hollow structures: Controlled synthesis and applications in energy storage and conversion. Adv Mater, 2017, 29: 1602914
26 Wang X, Feng J, Bai Y, *et al.* Synthesis, properties, and applications of hollow micro-/nanostructures. Chem Rev, 2016, 116: 10983–11060
27 Wu Q, Yang L, Wang X, *et al.* From carbon-based nanotubes to nanocages for advanced energy conversion and storage. Acc Chem Res, 2017, 50: 435–444
28 Yin Y, Rioux RM, Erdonmez CK, *et al.* Formation of hollow nanocrystals through the nanoscale Kirkendall effect. Science, 2004, 304: 711–714
29 Cao H, Qian X, Wang C, *et al.* High symmetric 18-facet polyhedron nanocrystals of Cu_7S_4 with a hollow nanocage. J Am Chem Soc, 2005, 127: 16024–16025
30 Wang X, Liao M, Zhong Y, *et al.* ZnO hollow spheres with double-yolk egg structure for high-performance photocatalysts and photodetectors. Adv Mater, 2012, 24: 3421–3425
31 Wu HL, Sato R, Yamaguchi A, *et al.* Formation of pseudomorphic nanocages from Cu_2O nanocrystals through anion exchange reactions. Science, 2016, 351: 1306–1310
32 Xiong S, Zeng HC. Serial ionic exchange for the synthesis of multishelled copper sulfide hollow spheres. Angew Chem Int Ed, 2012, 51: 949–952
33 Nai J, Tian Y, Guan X, *et al.* Pearson's principle inspired generalized strategy for the fabrication of metal hydroxide and oxide nanocages. J Am Chem Soc, 2013, 135: 16082–16091
34 Xia X, Wang Y, Ruditskiy A, *et al.* 25th anniversary article: galvanic replacement: a simple and versatile route to hollow nanostructures with tunable and well-controlled properties. Adv Mater, 2013, 25: 6313–6333
35 Oh MH, Yu T, Yu SH, *et al.* Galvanic replacement reactions in metal oxide nanocrystals. Science, 2013, 340: 964–968
36 Yang X, Fu J, Jin C, *et al.* Formation mechanism of $CaTiO_3$ hollow crystals with different microstructures. J Am Chem Soc, 2010, 132: 14279–14287
37 Yu XY, Feng Y, Jeon Y, *et al.* Formation of Ni-Co-MoS_2 nanoboxes with enhanced electrocatalytic activity for hydrogen evolution. Adv Mater, 2016, 28: 9006–9011
38 Deng J, Li H, Xiao J, *et al.* Triggering the electrocatalytic hydrogen evolution activity of the inert two-dimensional MoS_2 surface *via* single-atom metal doping. Energy Environ Sci, 2015, 8: 1594–1601
39 Sun X, Huo J, Yang Y, *et al.* The Co_3O_4 nanosheet array as support for MoS_2 as highly efficient electrocatalysts for hydrogen evolution reaction. J Energy Chem, 2017, 26: 1136–1139
40 Shen L, Yu L, Yu XY, *et al.* Self-templated formation of uniform $NiCo_2O_4$ hollow spheres with complex interior structures for lithium-ion batteries and supercapacitors. Angew Chem Int Ed, 2015, 54: 1868–1872
41 Zhao X, Yu R, Tang H, *et al.* Formation of septuple-shelled $(Co_{2/3}Mn_{1/3})(Co_{5/6}Mn_{1/6})_2O_4$ hollow spheres as electrode material for alkaline rechargeable battery. Adv Mater, 2017, 29: 1700550
42 Jiang J, Gao M, Sheng W, *et al.* Hollow Chevrel-phase $NiMo_3S_4$ for hydrogen evolution in alkaline electrolytes. Angew Chem Int Ed, 2016, 55: 15240–15245
43 Wang Y, Chen Z, Lei T, *et al.* Hollow $NiCo_2S_4$ nanospheres hy-

bridized with 3D hierarchical porous rGO/Fe_2O_3 composites toward high-performance energy storage device. Adv Energy Mater, 2018, 8: 1703453
44 Zhang DF, Zhang H, Guo L, *et al.* Delicate control of crystallographic facet-oriented Cu_2O nanocrystals and the correlated adsorption ability. J Mater Chem, 2009, 19: 5220–5225
45 Shang Y, Zhang D, Guo L. CuCl-intermediated construction of short-range-ordered Cu_2O mesoporous spheres with excellent adsorption performance. J Mater Chem, 2012, 22: 856–861
46 Miao R, Dutta B, Sahoo S, *et al.* Mesoporous iron sulfide for highly efficient electrocatalytic hydrogen evolution. J Am Chem Soc, 2017, 139: 13604–13607
47 Kresse G, Hafner J. *Ab initio* molecular dynamics for liquid metals. Phys Rev B, 1993, 47: 558–561
48 Kresse G, Hafner J. *Ab initio* molecular-dynamics simulation of the liquid-metal–amorphous-semiconductor transition in germanium. Phys Rev B, 1994, 49: 14251–14269
49 Kresse G, Furthmüller J. Efficient iterative schemes for *ab initio* total-energy calculations using a plane-wave basis set. Phys Rev B, 1996, 54: 11169–11186
50 Kresse G, Joubert D. From ultrasoft pseudopotentials to the projector augmented-wave method. Phys Rev B, 1999, 59: 1758–1775
51 Chen W, Chen H, Zhu H, *et al.* Solvothermal synthesis of ternary Cu_2MoS_4 nanosheets: Structural characterization at the atomic level. Small, 2014, 10: 4637–4644
52 Yu L, Xia BY, Wang X, *et al.* General formation of M-MoS_3 (M = Co, Ni) hollow structures with enhanced electrocatalytic activity for hydrogen evolution. Adv Mater, 2016, 28: 92–97
53 Tran PD, Nguyen M, Pramana SS, *et al.* Copper molybdenum sulfide: a new efficient electrocatalyst for hydrogen production from water. Energy Environ Sci, 2012, 5: 8912–8916
54 Tiwari AP, Kim D, Kim Y, *et al.* Highly active and stable layered ternary transition metal chalcogenide for hydrogen evolution reaction. Nano Energy, 2016, 28: 366–372
55 Liu W, Huang J, Yang Q, *et al.* Multi-shelled hollow metal-organic frameworks. Angew Chem Int Ed, 2017, 56: 5512–5516
56 Zhan G, Zeng HC. ZIF-67-derived nanoreactors for controlling product selectivity in CO_2 hydrogenation. ACS Catal, 2017, 7: 7509–7519
57 Zhang X, Zhao R, Wu Q, *et al.* Petal-like MoS_2 nanosheets space-confined in hollow mesoporous carbon spheres for enhanced lithium storage performance. ACS Nano, 2017, 11: 8429–8436
58 Yang G, Xu L, Chao Y, *et al.* Hollow MnO_2 as a tumor-microenvironment-responsive biodegradable nano-platform for combination therapy favoring antitumor immune responses. Nat Commun, 2017, 8: 902
59 Ma TY, Dai S, Jaroniec M, *et al.* Metal–organic framework derived hybrid Co_3O_4-carbon porous nanowire arrays as reversible oxygen evolution electrodes. J Am Chem Soc, 2014, 136: 13925–13931
60 Lu AY, Yang X, Tseng CC, *et al.* High-sulfur-vacancy amorphous molybdenum sulfide as a high current electrocatalyst in hydrogen evolution. Small, 2016, 12: 5530–5537
61 Brandão FD, Ribeiro GM, Vaz PH, *et al.* Identification of rhenium donors and sulfur vacancy acceptors in layered MoS_2 bulk samples. J Appl Phys, 2016, 119: 235701
62 Chae OB, Kim J, Park I, *et al.* Reversible lithium storage at highly populated vacant sites in an amorphous vanadium pentoxide electrode. Chem Mater, 2014, 26: 5874–5881
63 Li Y, Wang H, Xie L, *et al.* MoS_2 nanoparticles grown on graphene: An advanced catalyst for the hydrogen evolution reaction. J Am Chem Soc, 2011, 133: 7296–7299
64 Ma YY, Wu CX, Feng XJ, *et al.* Highly efficient hydrogen evolution from seawater by a low-cost and stable CoMoP@C electrocatalyst superior to Pt/C. Energy Environ Sci, 2017, 10: 788–798
65 Zhang J, Wang T, Liu P, *et al.* Engineering water dissociation sites in MoS_2 nanosheets for accelerated electrocatalytic hydrogen production. Energy Environ Sci, 2016, 9: 2789–2793

Acknowledgements This work was financially supported by the National Natural Science Foundation of China (51532001).

Author contributions Guo L and Yu J conceived the idea. Yu J carried out the synthesis, characterization, and electrocatalysis evaluation of the materials. Li A carried out the model construction and DFT calculations. Li L, Li X and Wang X helped with the characterization. All authors contributed to the data analysis and drafted the manuscript.

Conflict of interest The authors declare no conflict of interest.

Supplementary information Experimental details and supporting data are available in the online version of the paper.

Jian Yu received his BSc and MSc degrees from the School of Environmental and Chemical Engineering, Nanchang Hangkong University in 2012 and 2015, respectively. Now, he is a PhD candidate under the supervision of Prof. Lin Guo in the School of Chemistry, Beihang University. His research interest focuses on the synthesis of hollow porous nanomaterials and their applications in catalysis and energy.

Lin Guo received his PhD degree in Beijing University of Institute of Technology in 1997. Currently, he is a professor in the School of Chemistry, Beihang University. His research interests focus on the development of new methods for the synthesis of nano-structured materials and the characterization of their unique properties with high potential for future applications. He is a member of the Chinese Chemical Society, as well as the vice-dean of the School of Chemistry, Beihang University.

非晶Cu_2MoS_4纳米笼的形貌和结构工程用于高效电解水产氢

余建, 李安然, 李丽东, 李晓霞, 王晓天, 郭林*

摘要 非晶纳米材料因长程无序的原子排列，其形貌和结构的调控极具挑战性. 本文首次报道了一种可控自水解蚀刻-沉淀(SHEP)法，在常温常压下即可合成出空心多孔且形貌规则的非晶Cu_2MoS_4纳米笼(a-Cu_2MoS_4). 得益于其空心多孔结构和非晶的丰富硫缺陷，a-Cu_2MoS_4表现出比晶体相对物更强的析氢反应(HER)活性. 其中，壳厚度为20 nm的八面体a-Cu_2MoS_4表现出最好的HER活性：在10 mA cm^{-2}电流密度下，过电位仅为96 mV，塔菲尔斜率低至61 mV $decade^{-1}$；这主要是因为a-Cu_2MoS_4合适的厚度既保证了其表面的多孔性，又确保了其结构的稳定性. 本文提出的合成方法具有普适性，可扩展到更多的三元纳米笼材料的合成，为各种三元纳米笼的精确可控制备提供了新视角，并为开发高活性非晶催化剂开辟了新的途径.

